Int J Fract (2020) 224:67–82
https://doi.org/10.1007/s10704-020-00446-2

ORIGINAL PAPER

On the ductile rupture of 13% Cr-4% Ni martensitic stainless steels

Fayaz Foroozmehr · Philippe Bocher

Received: 20 August 2019 / Accepted: 1 April 2020 / Published online: 23 April 2020

Abstract Ductile rupture of 13% Cr-4% Ni martensitic stainless steels was examined during tension testing in order to better understand the role of second phase particles in these materials. SEM fracture surface examinations revealed that micro-voids were initiated from inclusions, and these inclusions were characterized from metallographic polished sections. Effect of stress triaxiality on the growth and impingement of the micro-voids were examined using a modified model of Rice and Tracey. In the case of the cast and wrought versions, the true fracture strains predicted for the measured stress triaxiality values were in a good agreement with the measured ones. For the weld metals, only the contribution of the micro-void growth cannot explain the experimental results, and it shows that the matrix properties such as austenite content and hardness of martensite play a significant contribution. The magnitude of the final stress triaxiality ratio measured after rupture was also related to the inclusion characteristics.

Keywords Stress triaxiality · Void growth · Fracture strain

F. Foroozmehr (✉)· P. Bocher
École de technologie supérieure (ÉTS), Montreal, QC H3C 1K3, Canada
e-mail: fayaz.foroozmehr.1@ens.etsmtl.ca;
f_foroozmehr@yahoo.com

P. Bocher
e-mail: philippe.bocher@etsmtl.ca

1 Introduction

13% Cr-4% Ni martensitic stainless steels possess high mechanical properties in terms of strength and toughness used to manufacture of hydraulic turbine runners (Amrei et al. 2016; Bilmes et al. 2000; Das et al. 2008; Thibault et al. 2009, 2010, 2011; Trudel et al. 2014). These hydroelectric runner components are usually assembled using flux-cored arc welding (FCAW) process. This is a high-quality welding process; however, the existence of defects such as inclusions or small cracks in a welded structure is inevitable, which can result in crack propagation during service. The unstable crack propagation of these alloys have been reported to always take place in a ductile manner, except the ones occurring at very low temperatures (− 75 °C or lower) (Foroozmehr et al. 2017). A way to better understand and predict the deformation behavior before rupture of this category of stainless steels is to correlate metallographic examination with their mechanical behavior.

Ductile rupture happens by nucleation and growth, and finally coalescence of micro-voids (Gurland and Plateau 1963; Pineau 2008). The mechanism involved is entitled "micro-void coalescence (MVC)". Second phase particles and inclusions are the principal source of micro-void nucleation (Anderson 2005). The growth of micro-voids is known to absorb the major part of the energy in ductile rupture (Campbell 2012). However, if only a small number of nucleation sites are available, important micro-voids growth will take place. If, on

the other hand, it occurs in large numbers, a premature coalescence will take place and the growth stage could be neglected (Broek 1971). Accordingly, the growth stage depends on the micro-void initiation sites density, and it can be said that ductile rupture is controlled by the nucleation of micro-voids (Broek 1971). In addition to the surface density of inclusions, the size, spacing, and volume fraction of these non-metallic particles is of great importance in ductile rupture (Foroozmehr et al. 2017).

Effects of the microstructural features, and especially the inclusion characteristics, on fracture of some steel alloys during ductile rupture were extensively examined in (Choudhary and Garrison 2010; Foroozmehr et al. 2017; Garrison 2007; Maloney and Garrison 2005; Maropoulos et al. 2004). It was shown that the non-metallic inclusions play the major role at the onset of rupture, and both the elongation at fracture or true fracture strain (ε_r) and the fracture toughness increase by increasing the spacing of inclusions. The size of inclusions is also of great importance as the larger is the inclusion size, the lower is the required nucleation stress and strain. In addition, the nature of the inclusions plays a role, as inclusions more resistant against rupture, and against micro-void formation result in higher fracture toughness. In addition, the austenite in 13% Cr-4% Ni martensitic stainless steels is mechanically unstable, improving the mechanical properties. This mechanically unstable austenite transforms into martensite under loading, increasing significantly the ductility (Bilmes et al. 2001; Folkhard and Rabensteiner 1988; Lippold and Kotecki 2005; Qiu et al. 2013). Zhang et al. (2015) showed that in 13% Cr-4% Ni martensitic stainless steels this transformation-induced plasticity (TRIP) effect continues until final rupture. Due to the volumetric expansion occurring during martensite formation, some compressive strains are produced, and may decelerate the nucleation and growth of micro-voids.

The growth of an isolated void with a cylindrical shape in a perfectly plastic matrix was modeled by McClintock (1968). Considering the growth of a spherical single void Rice and Tracey (1969) proposed a more realistic model still based on a perfectly plastic matrix:

$$\frac{dR}{R} = 0.283 \exp\left(\frac{3}{2}\frac{\sigma_m}{\sigma_y}\right) d\varepsilon_p \tag{1}$$

where R is the void radius, σ_m is the mean stress, σ_y is the yield stress of the material, and $d\varepsilon_p$ is the increment of equivalent plastic strain. Escatha and Devaux (1979) modified the model by replacing the yield stress (σ_y) by the von Mises equivalent stress (σ_{eq}). The ratio σ_m/σ_{eq} in the equation being equal to the stress triaxiality factor S_T, Huang (1991) modified the growth rate of the single void with respect to the stress triaxiality (S_T) as follows:

$$\frac{dR}{R} = 0.427\,(S_T)^{0.25} \exp\left(\frac{3}{2}S_T\right) d\varepsilon_p \quad \text{for } 1/3 \leqslant S_T \leqslant 1 \tag{2}$$

and

$$\frac{dR}{R} = 0.427 \exp\left(\frac{3}{2}S_T\right) d\varepsilon_p \quad \text{for } S_T \geqslant 1 \tag{3}$$

This model proposes an exponential relationship between the growth rate of the void and the stress triaxiality. In fact, the material in the necked region is highly stressed and should contract, while being surrounded by lower stressed material (Anderson 2005; Dieter 1986; Hertzberg 1996). This resistance of the material against contraction is called "constraint" (Brocks and Schmitt 1995), resulting to a triaxial stress state by producing radial and transversal stresses (Anderson 2005; Dieter 1986; Hertzberg 1996).

Using such an approach, the main purpose of this study is to examine the fracture behavior of 13% Cr-4% Ni martensitic stainless steels, focusing on the microstructural features and the stress triaxiality. Accordingly, the modified Rice and Tracey model by Huang is used. After a brief presentation of the materials (chemical composition and heat treatment), the experimental procedures used in this study is presented. Metallographic examinations including inclusion characterization analyses, tension tests, fractographic examinations, and XRD analyses are used to document the inclusion characteristics, the actual fracture surfaces of broken tension samples, and the austenite contents of the materials. The stress triaxialities calculated from the geometry of the necking region, are used to calculate the equivalent fracture strains (ε) based on the inclusion characteristics measured on the metallographic polished sections and the radius measurements made on the fracture surfaces. The results are then compared with the experimental data.

2 Materials and experimental procedures

Three different 13% Cr-4% Ni alloys were studied: one cast (CA6NM), one wrought (415), and one weld

metal (410NiMo), as provided in (Table 1). The expression "base metals" will be used to refer both CA6NM and 415 steels in order to differentiate these materials from the deposited weld metal. The base metals were tested in the tempered condition. The cast steel was austenitized at 1050 °C and tempered at 610 °C; the wrought one was austenitized at 1000 °C and tempered at 600 °C. Both steels were quenched in air. The weld metal block was deposited by flux-cored arc welding process (FCAW), and was tested in both, as-welded and heat-treated conditions (600 °C for 2 h). As seen in Table 1, the studied materials had similar chemical compositions, and were in the category of 13% Cr-4% Ni martensitic stainless steels.

Metallographic sections of the base and weld metals were polished to a mirror appearance using sand papers and diamond suspensions. The mirror polished surfaces were then examined by optical microscopy to study the defects such as porosity and inclusions existed in the microstructure of the tested materials. Five optical micrographs were taken randomly from all over the polished surfaces of each of the materials. In comparison to the base metals for which a low-level 50× magnification was used, a much larger magnification of 500× was needed for the characterization of the weld metal due to the small size of the inclusions. As a result, the examined surface was much smaller in the case of the weld metal; a total surface of 14 mm^2 versus 0.15 mm^2 was examined, respectively. The measured area fraction of inclusions were converted into the volume fraction of inclusions since the area fraction of the phase of interest measured on a section is equal to its volume fraction (ASM-Handbook 2004). In this study, the inclusion volume fractions were measured using an automatic image analyzer software (ImageJ) (ASM-Handbook 2004).

The surface densities of defects (N_A) were measured for each image, and then reported for a square centimeter. The equivalent circle radii of the measured defects were calculated and an average value was reported as the initial defect radius (R_0) for each of the materials. The defect spacing was calculated by the equation $S = 1.78R_0(V_v)^{-1/3}$, where V_v is the defect volume fraction, $R_0 = (\pi/4)H(R)$, and $H(R)$ is the harmonic mean of the measured defects radii (Garrison 2007).

To reveal the microstructures, the mirror polished surfaces were then etched using modified Fry's solution (150 mL distilled water, 1 g $CuCl_2$, 50 mL HNO_3, and 50 mL HCL) in a similar way reported in (Foroozmehr et al. 2017; Thibault et al. 2011).

Three tension tests per material/condition were carried out in accordance with ASTM E8/E8M (ASTM-International 2009) using a strain rate of $2.5 \times 10^{-4} s^{-1}$ at room temperature. The area section of the samples was about 20 mm^2 as smooth round bar specimens with a diameter of 5 mm were used. Up to necking, the stress triaxiality (S_T) is equal to 1/3 at the center of a round bar tension specimen. At the onset of necking, the stress triaxiality (S_T) increases continuously due to the increasing of the constraint (François et al. 2012). The stress triaxiality was calculated at the center of the necked region from the broken tension samples using Bridgman's relation (Bridgman 1952):

$$S_T = \frac{1}{3} + \ln\left(1 + \frac{r_0}{2\mathbb{R}}\right) \quad (4)$$

where r_0 is the radius of the necked region and $\mathbb{R}$ is the radius of curvature of necking at the moment of final rupture. These parameters were measured precisely on the images taken from the necked regions of the broken samples, using an image analyzer software "Image J".

The metallographic polished sections as well as the fracture surfaces were examined by scanning electron microscopy (SEM). At least 155 SEM micrographs were examined for each of the base and the weld metals. Inclusion radii were measured on the fracture surfaces of the tested materials. As automatic measurements were not possible in this case, inclusions were measured one by one manually using high magnifications to perform precise measurements. Note that the size of broken inclusions was ignored and only the intact ones were only considered for fracture surface measurements, introducing eventually an artifact. Therefore, in the condition in which a considerable number of large inclusions had been already fractured upon rupture, it is expected that the inclusion radius measured on the fracture surface is smaller than the actual ones.

As these materials can have austenite after tempering, the contents of this phase were measured by X-ray diffraction (XRD) using the Rietveld method (Young 1993). A Bruker D8 Advance diffractometer equipped with a copper tube and a nickel filter was used. Diffraction patterns were obtained in the range $40° < 2\theta < 140°$ with a step size of 0.05° (Thibault et al. 2011). The samples were cut by an automatic cut-off machine using 0.5 mm thick saw blades with a cut speed of 0.05 mm/s to minimize austenite transformation to martensite during the cutting process. Cut sur-

Table 1 Chemical compositions of the tested materials (wt%)

Designation	Cr	Ni	Mo	C	Mn	P	S	Si
CA6NM steel	12.79	3.49	0.55	0.016	0.50	0.019	0.007	0.26
415 steel	13.021	3.91	0.56	0.028	0.73	0.022	0.002	0.34
410NiMo weld metal	12.1	4.67	0.61	0.027	0.04	0.01	0.0093	0.48

Measurements were performed using inductively coupled plasma-emission atomic spectrometry (C and S were measured by combustion)

faces were ground by 1200 grit sand papers and etched in a 30% HCl + 30% HNO_3 + 40%H_2O solution for 10 min, then etched in HCl for 30 s. Three samples were prepared from each material to measure the initial austenite content.

3 Results

3.1 Inclusion characteristics

Examples of the analyzed optical micrographs taken from the metallographic polished sections of the studied materials are shown in Fig. 1a–c. The observed surfaces are perpendicular to the tension axis for the wrought steel (415) and the weld metal (410NiMo). The metallographic and tension samples were taken randomly in the case of the cast steel (CA6NM), whereas for the weld metal the tension direction was perpendicular to the welding direction. The measured particles were inclusions in all the three micrographs as verified by SEM. The lowest possible magnification was used for the base and weld metals in order to characterize the largest inclusions in each of the materials since the largest inclusions play the major role in ductile rupture.

The inclusion characteristics (surface density N_A, volume fraction V_v, radius R_0, and half of spacing S/2 of inclusions) of the base and weld metals measured from the optical micrographs are compiled in Table 2. Inclusions were not of similar size ranges in the microstructure of the base metals, and both very small and very large inclusions were found in the microstructures of CA6NM and 415 steels. In other words, no single normal distributions were found for these materials. On the contrary, the standard deviations of the half of inclusion spacing S/2 values are low for each of the tested materials, showing that the inclusion spacing is normally distributed in each case. The effect of inclusions of different size ranges were considered to shed light on the ductile fracture of the base metals. To this purpose, the average size of the small and large inclusions was reported and the median radius ($R_{0median}$) was used as a discriminating parameter. In the case of CA6NM steel, the median radius was equal to 3.73 μm, and for 415 steel it was of 2.73 μm. Note that the average value of the inclusions smaller or equal to the $R_{0median}$ will be referred as R_{0S}, and that of the ones larger than $R_{0median}$ as R_{0L}, in this study. On the other hand, the distribution of inclusions in the weld metal could be fit with a normal distribution and the mean inclusion radius is a good representative for all inclusions in this case.

Even of the significant error intervals, the characteristics of the cast material show systematically higher values than 415, except for inclusion spacing, for which equal values were obtained. Inclusions are at least five times smaller in the weld metal than those in the base metals. Similarly, the spacing of inclusions is at least 19 times smaller in the weld metal resulting in a surface density of all inclusions (N_A) about 800 times higher than in the base metals. The inclusion volume fraction (V_v) was also more than 5 times higher.

Inclusion size distributions of the metallographic polished sections are shown Fig. 2. In the case of the weld metal (410NiMo), almost all inclusions (more than 98%) measured on the metallographic polished sections are smaller than one micrometer in radius and the inclusion sizes cannot be ranked in a meaningful way. However, for the base metals (CA6NM and 415) it can be said that the median radius $R_{0median}$ classifies the results in two major size ranges i.e., R_{0S} and R_{0L} (as described in Table 2).

The microstructures of the tested materials are shown in Fig. 3a–e. The microstructures are mostly composed of lath martensite, but the stringers of delta ferrite can also be found in the microstructure of CA6NM and the weld metals for both as-welded and heat-treated conditions. The presence of delta ferrite is due to the concentration of some ferrite-promoting

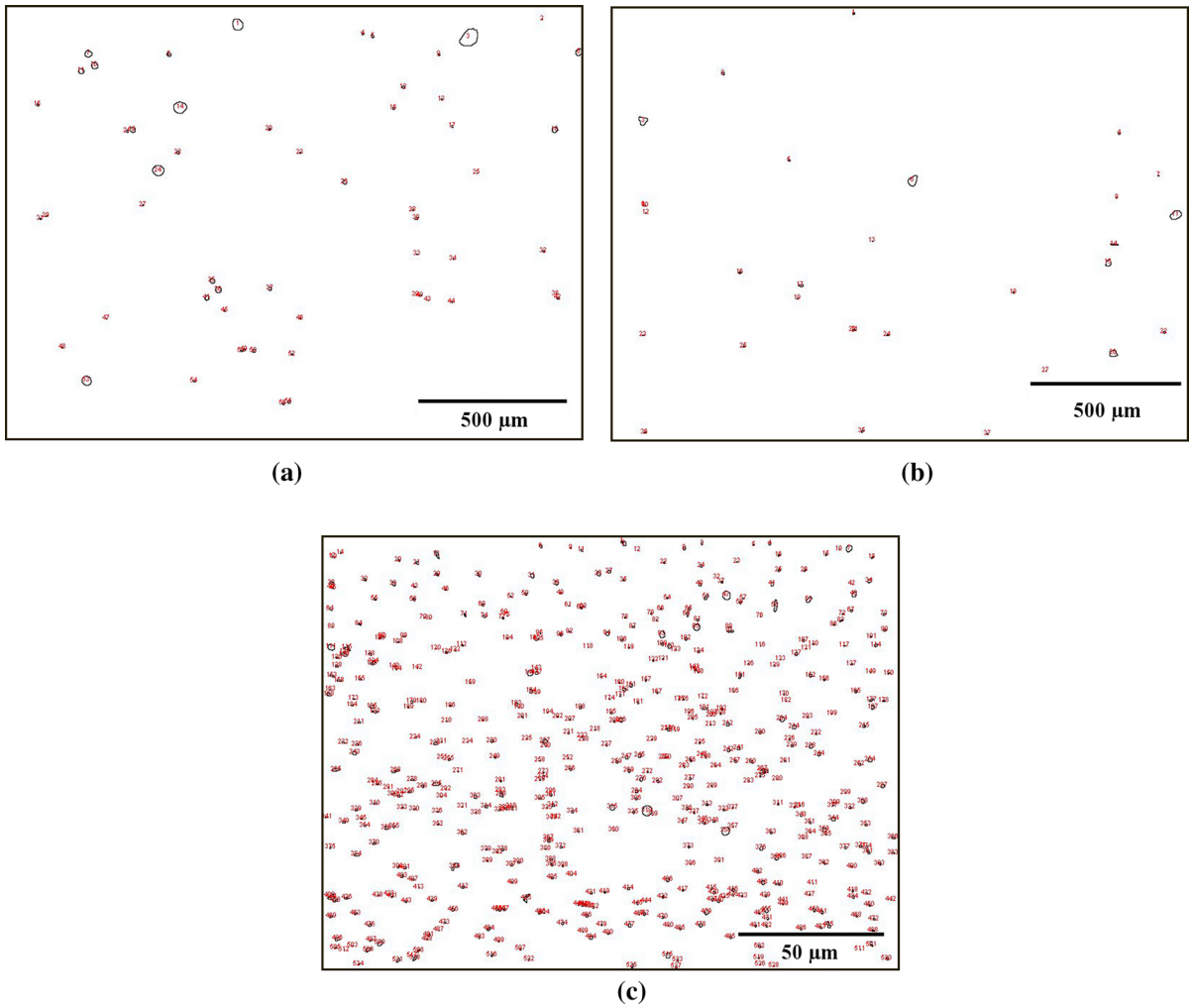

Fig. 1 Examples of processed images analyzed by automatic quantitative metallography: **a** CA6NM steel, **b** 415 steel, and **c** 410NiMo weld metal. The numbered circles are detected inclusions whose surfaces were measured on mirror polished surfaces

Table 2 Inclusion characteristics measured on the metallographic polished sections

Material	Measured inclusions	N_A (No./cm^2)	V_v (%)	Mean R_0 (µm)	Mean S/2 (µm)
CA6NM steel	R_0 (all)	1627 ± 368	0.22 ± 0.12	4.99 ± 4.31	18.53 ± 2.86
	R^a_{0S}	873 ± 232	0.02 ± 0.01	2.63 ± 0.79	28.27 ± 2.50
	R^a_{0L}	754 ± 176	0.20 ± 0.11	7.73 ± 5.05	35.88 ± 3.35
415 steel	R_0 (all)	1211 ± 242	0.09 ± 0.02	3.59 ± 3.21	18.02 ± 1.84
	R^b_{0S}	695 ± 208	0.01 ± 0	1.91 ± 0.52	28.78 ± 3.06
	R^b_{0L}	516 ± 180	0.08 ± 0.02	5.69 ± 3.96	35.02 ± 2.22
410NiMo weld metal	R_0 (all)	$(1.29 \pm 0.25) \times 10^6$	1.10 ± 0.14	0.38 ± 0.24	0.94 ± 0.05

R_{0S} represents $R_0 \leq R_{0median}$; R_{0L} represents $R_0 > R_{0median}$
[a] $R_{0median}$ is equal to 3.73 µm for CA6NM steel
[b] $R_{0median}$ is equal to 2.73 µm for 415 steel

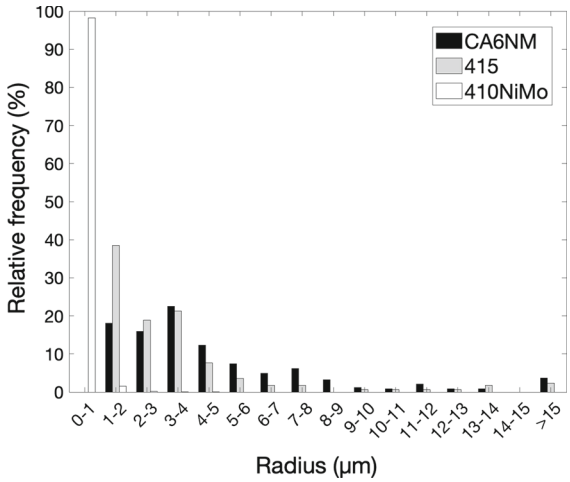

Fig. 2 Inclusion size distributions measured on metallographic polished sections

elements (especially Cr) as reported in (Folkhard and Rabensteiner 1988; Lippold and Kotecki 2005). The stringers of delta ferrite are shown by the black arrows in the microstructure of CA6NM (Fig. 3a) and in that of as-welded material (Fig. 3d). In the case of the weld metal, the stringers of delta ferrite are narrow and trapped in the former Widmanstätten austenite boundaries. This type of the delta ferrite is typical of such welded microstructures as reported in (Carrouge 2002) and (Amrei et al. 2016). Very fine inclusions in black closely dispersed in the microstructure are also seen. The microstructure of the tempered martensite shown in Fig. 3e displays a stronger contrast than that of fresh martensite (Fig. 3c). The austenite islets cannot be observed in these micrographs, requiring much higher magnifications. It is the concentration of austenite-promoting elements (especially Ni) in austenite during intercritical heat treatment that stabilizes this phase at room temperature (Folkhard and Rabensteiner 1988; Lippold and Kotecki 2005).

3.2 Ductile rupture

3.2.1 Measured deformations during tension testing

The engineering stress–strain curves of the tested materials were converted to the true ones until the onset of necking, as shown in Fig. 4. The yield (σ_y) and ultimate tension strengths (σ_{UTS}), true strain before necking (ε_{bn}), the true fracture strain (ε_r), the fracture strain after necking (ε_n) (which is the difference of ε_r minus ε_{bn}), and the austenite contents (γ_0) of the tested materials are provided in Table 3. The ε_{bn}, ε_r, and ε_n values were calculated using the following equations (Dieter 1986):

$$\varepsilon_{bn} = \ln\,(1+e) \tag{5}$$

where "e" is the engineering strain, and:

$$\varepsilon_r = 2\,\ln\left(\frac{D_0}{D}\right) \tag{6}$$

where D is the final radius, and D_0 is the initial radius of the tension specimen, and:

$$\varepsilon_n = \varepsilon_r - \varepsilon_{bn} \tag{7}$$

As provided in Table 3, the weld metals undergo higher yield and ultimate tension strengths than the base metals, but experience lower ductility. On the other hand, the CA6NM steel is the least resistant, but reaches high rupture strain. The heat-treatment at 600 °C for 2 h has improved the ε_n deformation, maintaining approximately the same yield strength (the difference between the yield strength of these two metallurgical states is only about 2%). For both base metals similar amounts of deformation took place before necking (ε_{bn}). The heat-treated weld metal underwent 75% higher deformation before necking than the as-welded one. In the case of the true fracture strains (ε_r), 415 steel underwent the largest one. Its ε_r deformation was 23% higher than the CA6NM steel, and 38% higher than the weld metals.

As the base metals underwent equal ε_{bn} deformations (Table 3), it can be said that differences in the ε_r and ε_n deformations between CA6NM and 415 steels are mainly due to their damaging process after necking, i.e., their different inclusion characteristics (Tables 2 and 4). On the other hand, the differences between the as-welded and heat-treated weld metals can be related to their differences in term of martensite and the austenite contents since they have similar inclusion characteristics. Therefore, the softer tempered martensite of the heat-treated material together with four times higher austenite content introducing TRIP effect resulted in higher ε_{bn} and ε_r values.

3.2.2 Fracture surfaces

Fracture surface examinations using SEM showed that fracture occurred by the mechanism of micro-void coalescence (MVC) for all metals, but the contribution of

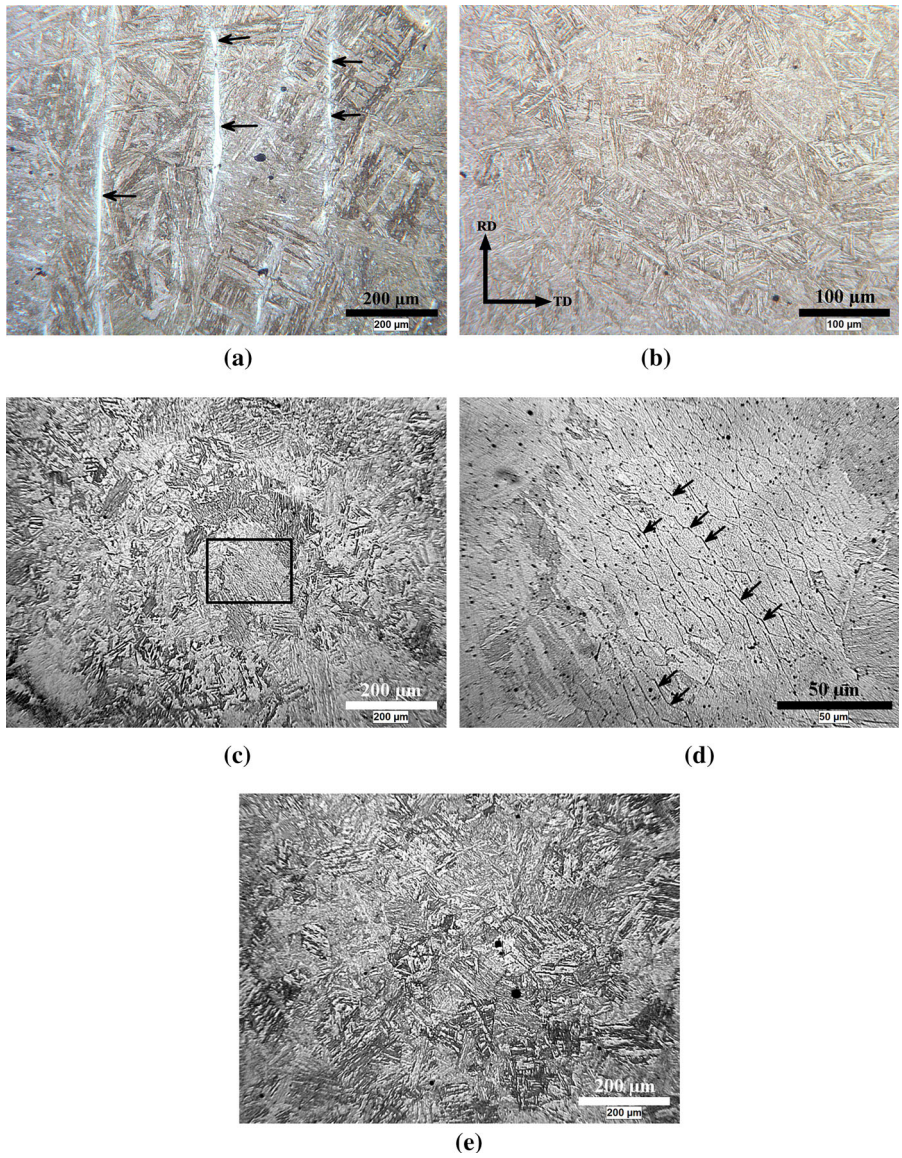

Fig. 3 Optical Microstructures of the tested materials: **a** CA6NM, **b** 415, **c** 410NiMo-AW, **d** enlargement of the outlined area by the black rectangle in **c**, and **e** 410NiMo-HT. The black notched arrows in **a** and **d** show the stringers of delta ferrite. In **b**, RD and TD represent the Rolling Direction and Transverse Direction, respectively

inclusions to rupture was significantly different from one metal to the next. Large inclusions were found in large number on the fracture surfaces of CA6NM steel, while small ones were reported for 415 steel. On the other hand, almost all inclusions observed on the fracture surfaces of the weld material, both as-welded and heat-treated conditions, were of the same size and the occurrence of larger inclusions was negligible. The nature of inclusions were also examined using Energy Dispersive X-ray (EDX) spectroscopy as reported in the previous work (Foroozmehr et al. 2017). In addition, it should be noted that no evidence of the presence of delta ferrite or large chromium carbides that may be formed in this phase (Schäfer 1998) were found on the fracture surfaces. Therefore, it can be concluded that the trace of delta ferrite does not affect the fracture of these alloys.

Typical examples of fracture surfaces are shown in Fig. 5. Large inclusions of more than 5 µm in radius are indicated by black arrows in the CA6NM fracture surface in Fig. 5a. In addition, numerous inclusions were found broken in the fracture surface of CA6NM steel. These large/broken inclusions are the basis of premature micro-void formations since lower strains are

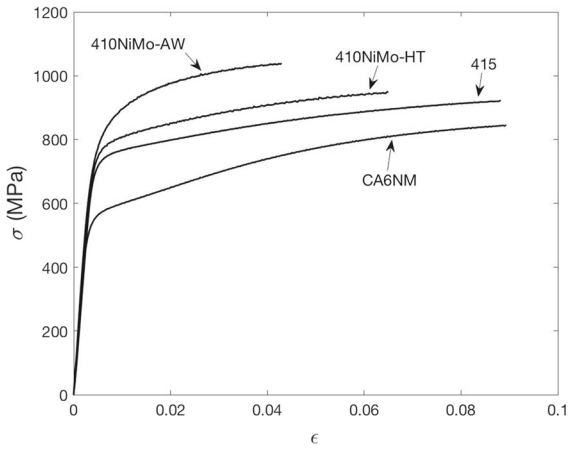

Fig. 4 Typical σ-ε curves of the tested materials. Only one curve per material is shown; however, three tests were performed on each material

needed than those required from smaller/intact inclusions to initiate micro-voids (Anderson 2005; Cox and Low 1974; Gurland and Plateau 1963). As shown by the outline filled black ellipse in Fig. 5a, premature micro-voids led to the formation of very large dimples (a final radius up to 55 μm at the moment of rupture). An example of a large dimple formed by a large fractured inclusion on CA6NM fracture surface is displayed in Fig. 5b.

In the case of 415 steel, the fracture appearance looks more complicated than that of CA6NM steel. As seen in Fig. 5c, the fracture surface is rougher and many small voids are found. Fig. 5d is a higher magnification micrograph of the black rectangle shown in Fig. 5c, showing some of the initially nucleated micro-voids by the black arrows. The very small voids found in this figure are making angles of about 40° with loading axis (shown by the black arrows) and correspond to what was called "void sheets" (Benzerga and Leblond 2010; Cox and Low 1974; Rogers 1960). The formation of these void sheets results in a considerable number of secondary cracks. If at the early stage of necking micro-voids are initiated on larger inclusions as lower deformations are required, the final rupture is controlled by void sheeting between these large micro-voids. They form when the constraint reaches a critical value in shear bands. These initial micro-voids are similar to the ones formed in CA6NM; however, the growth of the micro-voids is interrupted by the formation of the void sheets in this case as there are only few available micro-void nucleation sites of this type in the material. In addition, the nucleation sites of the micro-voids are also different in CA6NM and 415 steels as micro-voids were formed on small/intact inclusions in 415. Therefore, since there are not enough inclusions to initiate micro-voids homogeneously in the material, void sheets are formed at high stress/strain levels as the constraint get increased by necking. The mean radius of the initially nucleated micro-voids at the moment of void sheeting R_{vs} is equal to 6.36 μm ± 2.03 μm for 35 micro-voids on 415 steel fracture surfaces. As the density of micro-voids varies from one location to another, secondary cracks are generated to connect the region with higher density of formed micro-voids, completing the final coalescence.

On the other hand, in the as-welded material (410NiMo-AW) the inclusions and the corresponded dimples are approximately of similar sizes as can be seen in Fig. 5e. Some inclusions are shown by the black arrows in this micrograph. The fracture appearance of the heat-treated material was very similar as that of the as-welded one.

Table 4 provides the mean value of the inclusion radius measured from the fracture surfaces of each of the tested materials. In the case of the base metals, relatively large standard deviations show that the inclusion sizes measured on fracture surfaces cannot be properly described by normal distributions. However, comparing these average values with inclusion sizes measured on the metallographic polished sections (Table 2) can adequately demonstrate the micromechanical processes involved in each case: the inclusions larger than the median radius $R_{0median}$ initiate micro-voids in CA6NM, while this is the case of smaller ones in 415 steel. Inclusions found on the fracture surfaces are at least four times larger for the base metals compared to the weld metals. In addition, the mean inclusion radius of CA6NM steel was about 3.5 times larger than that of 415 steel. Inclusions had a similar size for both as-welded and heat-treated materials. The stress triaxialities at the center of the necked region measured from broken tension samples (using Eq. (4)) was also added to this table. The stress triaxialities were higher for the base metals.

In order to shed light on the inclusion contribution to rupture, the inclusion radius measured after rupture R_0' (Table 4) is compared with the ones measured on the metallographic polished section of the material (Table 2). In the case of CA6NM steel, the R_0' is close to the R_{0L} (Table 2) indicating that large inclusions

Table 3 Tension properties as well as austenite contents of the tested materials

Designation	σ_y (MPa)	σ_{UTS} (MPa)	ε_{bn}^{a}	ε_r	ε_n	γ_0 (%)[b]
CA6NM steel	575 ± 13.2	769 ± 7.4	0.09	0.99 ± 0.11	0.90	19.1 ± 6.4
415 steel	725 ± 0	843 ± 3.7	0.09	1.22 ± 0.06	1.13	19.5 ± 2.2
410NiMo-AW	783 ± 5.8	1007 ± 10.3	0.04	0.64 ± 0.04	0.60	2.4 ± 1.0
410NiMo-HT	765 ± 5	895 ± 4	0.07	0.75 ± 0.08	0.68	10.0 ± 0.6

[a]Equal ε_{bn} deformations were obtained for each of the tests performed on each material.
[b]Austenite percentages

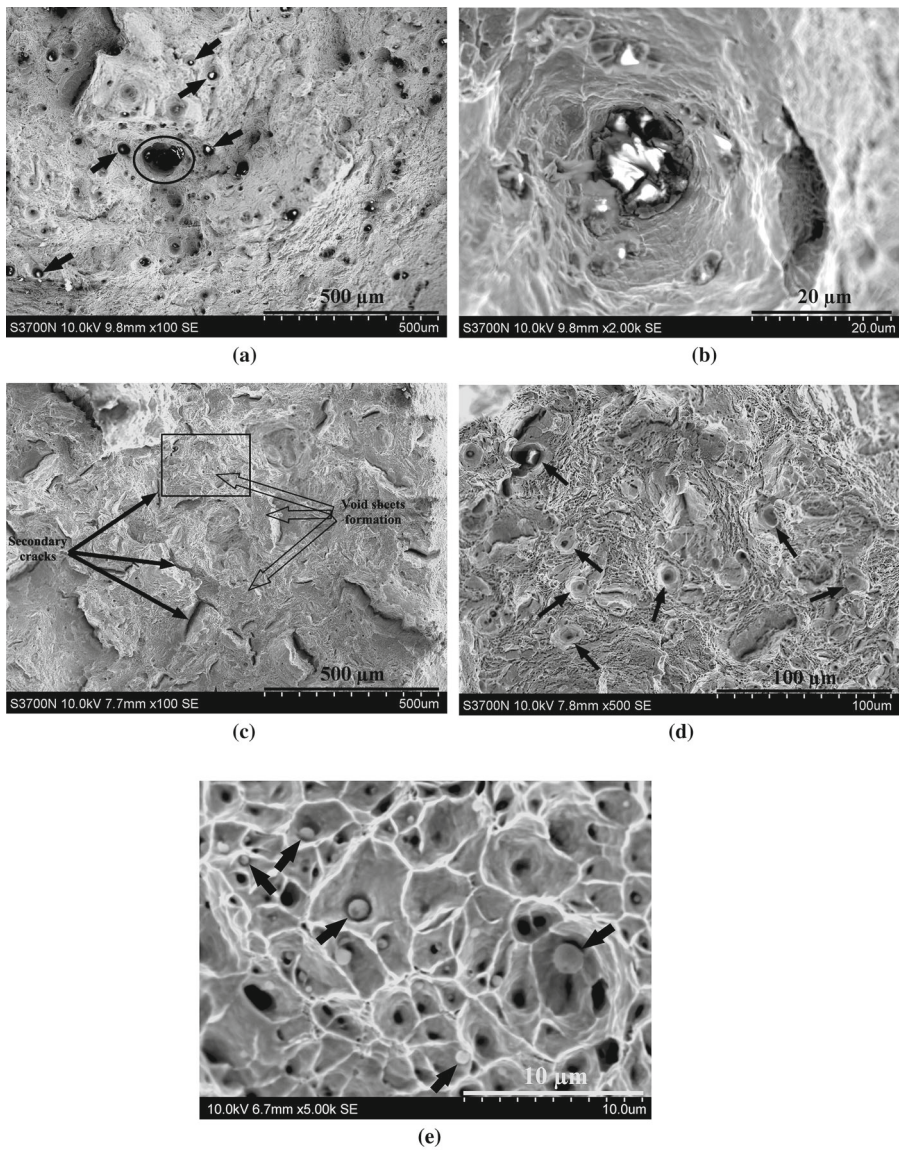

Fig. 5 Examples of SEM micrograph of the tested materials: CA6NM at **a** $\times 100$, and **b** $\times 2000$ magnifications, **c** 415 steel at $\times 100$ magnification, **d** the region shown by the black rectangle in **c**, and **e** 410NiMo-AW at $\times 5000$ magnification. In **a** some inclusions larger than 5 µm in radius are shown by the black arrows, and a very large dimple of 55 µm in radius formed before total breakdown of specimen is shown by the outline filled black ellipse. In **c** the filled arrows show some secondary cracks, and some facets formed by void sheeting are shown by the outline filled arrows. In **d** some initially nucleated micro-voids are shown by the black arrows. In **e** some inclusions are also shown by the black arrows. Note that loading axis is perpendicular to all the fracture surfaces shown in this figure

Table 4 Mean inclusions radii measured on tension fracture surfaces and stress triaxialities at the center of the necked region obtained from broken tension specimens

Material	R'_0 (μm)	S_T
CA6NM steel	6.23 ± 4.15	0.71 ± 0.02
415 steel	1.8 ± 1.12	0.77 ± 0.04
410NiMo-AW	0.43 ± 0.24	0.64 ± 0.04
410NiMo-HT	0.43 ± 0.14	0.66 ± 0.05

played the major role in the rupture of this alloy. On the other hand, in 415 steel the R'_0 is very close to the average radius of small inclusions suggesting that it is the local inclusion density that controlled the fracture mechanism, and the contribution of large inclusions is negligible.

In the welded materials, the difference between the mean radius of inclusions measured on the metallographic polished section and that measured on the fracture surfaces is negligible. This is true for both as-welded and heat-treated conditions. Accordingly, it can be said that all inclusions observed on the metallographic polished section of the weld metal had the same chance to initiate micro-voids if necking happens in that region.

3.2.3 Fracture strain estimation

After necking, the smooth tension sample can be considered as a notched bar with a small radius equivalent to the necked region r_0 and the radius of curvature of necking $\mathbb{R}$. In fact, the variation in the stress triaxiality from the onset of necking until final rupture was not considered in the model of Rice and Tracey, and it was considered constant during necking (Shi 1989). As necking is due to mechanical instability, and that void nucleation and growth take place at the last stage of fracture (way after necking, when the stress triaxiality S_T reaches high values), it was assumed that the growth and coalescence of the initially nucleated micro-voids occur rapidly just before rupture. The necked region radius r_0 and the curvature radius of necking $\mathbb{R}$ are thus assumed constant during crack nucleation and propagation. With that hypothesis, rupture takes place under constant stress triaxilaity ratio S_T. Both final rupture and interaction between voids were not considered in the model of Rice and Tracey (Eq. (1)). To remedy these problems, the final void radius at the moment of rupture was considered as fracture criterion in the integrated form of the modified Rice and Tracey model (Eq. (8)). That is to say, the interaction between voids is also considered. Accordingly, the fracture strain after necking (ε_n) can be estimated by integrating Eq. (2) as a function of the void radius (R) for a constant S_T. The value of the calculated fracture strain after necking ε'_n is then equal to:

$$\varepsilon'_n = 2.342\, S_T^{(-1/4)} \ln\left(\frac{R_f}{R_i}\right) \exp\left(-\frac{3}{2} S_T\right) \tag{8}$$

where ε'_n is the equivalent fracture strain, S_T is the stress triaxiality during necking, R_i and R_f are the initial and final void radius, respectively (the Eq. (3) was ignored as the measured and calculated stress triaxiality values are lower than one in this study). As final rupture takes place by the impingement of the micro-voids, only the behavior of an isolated void ($\ln(R_f/R_i)$) can be considered to estimate the equivalent fracture strain, and the plastic deformation that is required for the nucleation of micro-voids once necking has taken place is neglected. The obtained values can then be compared with the experimental results given by ε_n values provided in Table 3.

According to the Eq. (8), the initial and final radius of the voids are very important in dimpled rupture and different fracture strains can be considered based on the inclusion characteristics provided from the metallographic polished sections (Table 2), or the average inclusion radius measured on the fracture surfaces (Table 4).

Based on the fracture surface observations (Sect. 3.2.2), the inclusions contributing the micro-void coalescence (MVC) are different from one material to the next: Inclusions larger and smaller than the median radius played the major role in the rupture of CA6NM and 415 steels, respectively, and all inclusions contributed to rupture for both weld metals conditions. As a consequence, the R_{0L} and R_{0S} values (Table 2) are considered as the initial void radius R_i in CA6NM and

415, respectively. Again, based on the fractographic considerations, the final void radius in the MVC mechanism was estimated as the average value of the spacing of larger inclusions (R_{0L}) in CA6NM, and that of the smaller ones (R_{0S}) in 415.

The estimated ε_n values are reported in Table 5 for the S_T values obtained from broken tension samples (Table 4). Higher deformations than the measured ones are obtained. These values are 50% and 89% higher for CA6NM and 415 steels, respectively. It is most likely that the final radius of the micro-voids (R_f) was overestimated by considering that only large or small inclusions play a role in the MVC mechanism in CA6NM and 415 steels, respectively.

As the coalescence is occurring by impingement of the micro-voids formed on both small and large inclusions, a more realistic estimation can be obtained by considering the inclusion radius measured on the fracture surfaces R'_0 as the initial micro-void radius for both steels (Table 4). The final void radius R_f in CA6NM is to consider half of spacing of all inclusions S/2 (Table 2). This hypothesis comes from the observation that fracture surfaces of CA6NM steel are composed of both small and large dimples (Fig. 5a). The growth of the micro-voids initially nucleated on large inclusions is limited by the onset of micro-voids from small inclusions in the ligaments when stress and constraint increase. In the case of 415, the actual radius measured on 415 fracture surfaces (see Sect. 3.2.2) and equivalent to the R_{vs} at which void sheets take place is considered as R_f. The ε'_n values calculated based on these assumptions are reported in Table 6. The results show better prediction of the ε_n deformations, especially for CA6NM as with these asssumptions, micro-voids were nucleated on both large and small inclusions and not only on the large ones. In the case of 415, replacing the R_f value by the measured R_{vs} results in an underestimation of the ε_n deformation. This underestimation suggests that the formation of void sheets stops the growth of micro-voids, and the deformation resulting from void sheeting (ε_{vs}) is negligible. Accordingly, comparing the ε'_n deformations predicted in Tables 5 and 6 for 415, it is possible to state that the failure in this alloy takes place by the impingement of the micro-voids formed on smaller inclusions. It can be said also that the formation of void sheets results in a decrease of ε_n deformation as it dramatically accelerates the damage.

For the weld metals, all inclusions were in the similar size range, and additionally all of them contributed to rupture. Therefore, the measured inclusion radius from fracture surface R'_0 (Table 4) and half of the mean spacing of all inclusions S/2 (Table 2) are considered as R_0 and R_f values, respectively. Predicted ε'_n deformations of the weld metals are provided in Table 7. The predicted ε'_n deformation can be qualified as overestimated but acceptable for the heat-treated material, whereas the error is quite significant for the as-welded condition. The heat treatment has a negligible effect on the yield strength of the weld metal (Table 3). The characteristics of the inclusions being the same for these metallurgical conditions and the measured stress triaxialities were similar, Eq. (8) predicts that the ε'_n deformation of the heat-treated material is about 4% lower than that of the as-welded one, but the measured ε_n is 13% higher for this metallurgical condition compared to that of the as-welded one. It shows that microstructural features other than the void radius i.e., the austenite transforming into martensite by TRIP and the softer tempered martensitic matrix play a role in ductile fracture behavior of the weld metal.

It is interesting to look at the effect of the different void radii defined in this paper on the resultant stress triaxialities as based on the modified Rice and Tracey model. Equation (8) was used to calculate the stress triaxiality values using the R_i and R_f values defined in Tables 5 and 6 for the base metals, and those defined in Table 7 for the weld metals using the measured ε_n deformations. Table 8 reports the resulted S_T values. For each of the base metals, two series of results are reported: the first row is attributed to the R_{0L} in the case of CA6NM and R_{0S} for 415. The second row provides the information obtained from fracture surface observations for both these steels. By contrast, the same critical micro-void growth rate was considered for both as-welded and heat-treated conditions.

When using R_{0L} and R_{0S} as the microstructural characteristics, the S_T values obtained are highly overestimated suggesting that the final micro-void radii were overestimated, resulting in much higher constraints and stress triaxiality values at rupture. However, as the growth of initially nucleated micro-voids were limited by micro-void initiation on small inclusions in CA6NM and void sheeting in 415, R_f values was redefined as the S/2 (half of spacing of all inclusions reported in Table 2) for CA6NM and R_{vs} (actual radius of the micro-voids at the moment of void sheeting) in 415 steel. This led

Table 5 Predicted ε'_n deformations of the base metals based on the inclusions larger and smaller than the $R_{0median}$ value in CA6NM, and 415, respectively, measured on the metallographic polished sections

Material	S_T	R_i (μm)	R_f (μm)	ε'_n	ε_n	Relative difference (%)
CA6NM steel	0.71	7.73	35.85	1.35	0.9	+ 50
415 steel	0.77	1.91	28.78	2.14	1.13	+ 89

Table 6 Predicted ε'_n deformations of the base metals based on the inclusion size measurements on the fracture surfaces R'_0 as the initial void radius R, as well as half of spacing of all inclusions in CA6NM and the R_{vs} value in 415 as the final void radius R_f

Material	S_T	R'_0 (μm)	R_f (μm)	ε'_n	ε_n	Relative difference (%)
CA6NM steel	0.71	6.23	18.53	0.96	0.9	+ 7
415 steel	0.77	1.8	6.36	0.99	1.13	− 12

Table 7 Predicted ε'_n deformations of the weld metals based on the R'_0 and the mean value of half of spacing of all inclusions measured on the metallographic polished sections

Material	S_T	R'_0 (μm)	R_f (μm)	ε'_n	ε_n	Relative difference (%)
410NiMo-AW	0.64	0.43	0.94	0.79	0.60	32
410NiMo-HT	0.66	0.43	0.94	0.76	0.68	12

to better S_T predictions. In other words, these fracture micromechanical processes were activated when the constraint and stress triaxiality reach their critical values, promoting final rupture.

For the as-welded material, the difference between the calculated and measured stress triaxialities is significant (22%), but this difference decreased significantly in the heat-treated material with only 9% higher than the measured one. As the critical micro-void growth is the same between both as-welded and heat-treated conditions (Table 7), it can be concluded that some microstructural features other than the initial and final radius of the micro-voids influence the material behavior during necking.

4 Discussion

The available data set gives the opportunity to study the effect of the matrix microstructural features i.e., the austenite and martensite on fracture behavior of the alloys. The microstructures of the tested materials have different amounts of austenite, resulting in the possibility for some TRIP to take place until final rupture for the alloys containing the larger amounts. During TRIP, austenite transforms into martensite under loading, enhancing strain hardening even at late stage of deformation. This effect is known to delay void growth and increase the ductility of the alloy (Antolovich 1996; Zhang et al. 2015). In addition, the volume change associated with the transformation of austenite to martensite also retard the nucleation of micro-voids by producing compressive stresses, and thus requiring higher ε_{bn} deformations for final rupture (Antolovich 1996; Zhang et al. 2015). Therefore, the higher austenite contents of the CA6NM and 415 alloys (Table 3) enable the base metals to undergo higher ε_{bn} and ε_n deformations. The austenite content of the heat-treated weld material does not play a significant role in the MVC mechanism because the number of void nucleation site is very high compared to the number of austenite islets.

For the base metals, one can assume that both steels have similar TRIP properties as they have undergone similar heat treatments, and the austenite content is approximately the same (19% as provided in Table 3). The martensitic matrix in the 415 steel has a higher strength than the CA6NM due to high carbon content, but it can be assumed that the TRIP effect would result in equal increase in their deformation behaviors as both steels undergo the same deformation before necking ($\varepsilon_{bn} = 0.09$). After necking, they underwent different deformation paths (Table 3) and their critical

void growths (R_f/R_i) are of different natures (Table 4). The difference between their fracture strains is related to their different inclusion characteristics, which lead to different fracture micromechanical processes. In the case of the weld metal, the metastable austenite contents are different between the as-welded and heat-treated conditions (Table 3) and efficient TRIP can occur only in the heat-treated condition. This behavior explains the larger ε_n deformation after necking as TRIP in this condition is active until final rupture (Zhang et al. 2015).

Comparing the true strains after necking ε_n provided in Table 3 shows that 415 steel is the most ductile material, having an ε_n deformation of about 1.13, at least 26% and 66% larger than those of CA6NM and the weld metals, respectively. These different ε_n deformations can be explained by their various inclusion characteristics and metastable austenite contents, resulting in different abilities for void growth once mechanical instability has initiated necking. The void growth amounts taking place during necking, provided by $\ln(R_f/R_i)$, are equal to 1.26, 1.09, and 0.78 for 415, CA6NM, and the weld metals, respectively. These values show a correlation between the void growth and the true strains after necking: the larger void growth, the larger ε_n. Similarly, larger stress triaxiality values are found for larger ε_n (Table 4), i.e., larger stress triaxiality ratios are required for rupture to be occurred.

The presence of metastable austenite can also play a role in the damage mechanism, but in the case of 415 and CA6NM steels they have similar austenite content (Table 3) and it can be concluded that the 26% higher ε_n deformation of 415 steel compared to CA6NM is mostly due to 16% higher ability to growth void before failure.

Inversely, both 410NiMo-AW and 410NiMo-HT materials underwent the same amount of void growth (Table 2), but the metastable austenite content found in the heat-treated material together with the softer tempered martensite has the ability to increase by 13% the deformation after necking ε_n.

The differences in necking strains of the various steels are explained based on the experimental results and physical arguments. Even if the integrated form of the modified model of Rice and Tracey (Eq. (8)) presents some limitations as one needs to assume that void nucleation and coalescence take place at the end of the necking process and that the triaxiality state does not change, this model allows determining the total amount of the void growth taking place at the final rupture using the natural logarithm of the R_f/R_i ratio. This simplified approach may not represent adequately the complexity of the mechanisms happening after necking, but it has the advantage to differentiate the amounts of void growth in the tested materials and discriminate the related fracture micromechanics during necking as discussed below.

While conventional impingement of the initiated micro-voids was observed in both materials, void sheets were also observed in 415 steel. The consequence of void sheet formation is a lower constraint at rupture. The void sheets formed as an alternative way to adapt to the constraint as micro-void formation on the smaller inclusions would require much higher constraints. In fact, some regions of the microstructure present a low density of small inclusions (Fig. 5c). In other words, void sheeting resulted in a lower stress triaxiality than the expected one (by about 40%) if the final radius of the initially nucleated micro-voids is decreased by at least 75% compared to the expected value. The case of CA6NM steel is less straightforward if only large inclusions (R_{0L}) are considered to play a role in rupture. A 31% higher stress triaxiality value was obtained according to the modified model of Rice and Tracey. However, while the S_T value increases after necking, the nucleation process activates small inclusions, reducing by about 50% the final radius of the cavities (R_f). An R_f value equal to half of the mean spacing of all inclusions resulted in a precise S_T (Table 8) prediction, showing that small inclusions do contribute to rupture.

The weld metals ruptured at nearly the same low triaxiality values (Table 8). The predicted S_T values are overestimated for both cases, but the prediction error is lower for the heat-treated material (9% vs. 22%). The lower S_T prediction error for the heat-treated material may be due to efficient TRIP and the softer matrix as discussed earlier, but it could also be due to some limitations in the Rice and Tracey model, even in its modified form. Helbert and coworkers (Helbert et al. 1996) have showed that ductile rupture can hardly be expressed by the Rice and Tracey model when the nucleation of micro-voids occurs in very large numbers under a low stress triaxiality and low plastic deformation. This is because nucleation of micro-voids plays a major role than growth: only the growth stage of one void cannot capture the actual failure process. This limitation would be even more dramatic for the as-welded material due to its low ductility. Therefore, it is possible

Table 8 Calculated stress triaxialities for different initial radius R_i and final radius R_f of micro-voids defined in Tables 5, 6, and 7, and measured ε_n deformations

Material	R_i (μm)	R_f (μm)	ε_n	Calculated S_T	Measured S_T	Relative difference (%)
CA6NM steel	7.73	35.83	0.90	0.93	0.71	+31
	6.23	18.53		0.74		+4
415 steel	1.91	28.78	1.13	1.13	0.77	+47
	1.8	6.36		0.70		− 9
410NiMo-AW	0.43	0.94	0.60	0.78	0.64	+22
410NiMo-HT	0.43	0.94	0.68	0.72	0.66	+9

that the fracture behavior of the weld metal cannot be expressed by the S_T-void growth rate relationship defined in the modified model of Rice and Tracey. In the case of the base metals, the nucleation sites (inclusions) were much less numerous (the inclusion spacing is about 20 times higher than in the weld materials) resulting in a significant micro-void growth for each void, justifying the ability for the modified Rice and Tracey model to describe their fracture behavior.

Finally, it is interesting to shed light on the stress triaxiality ratios S_T measured on broken tension samples. Among the three heat-treated materials, the highest S_T value was produced in 415 steel for which the critical micro-void growth rate is the highest one (despite void sheets formation at a later stage of the fracture process). The impingement of the nucleated micro-voids occurred at a lower S_T ratio in the CA6NM steel because the critical micro-void growth is 16% lower, resulting in a lower ε_n. Finally, the weld metals have similar low S_T values, not affected by the different matrix properties. Accordingly, the lower S_T value of the heat-treated weld metal compared to the base metals was not due to its lower austenite content (being half that in the base metals) or higher martensite strength, but rather by its high, small size inclusion density. Therefore, the magnitude of the stress triaxiality ratio due to necking is related to the inclusion features rather than the matrix properties. It shows that in order to develop a model describing precisely ductile fracture behavior of the material, the inclusion characteristics and especially the size and spacing of inclusions should be also considered. In addition, the inclusion spacing in the weld metal is so small that the growth of the micro-voids is negligible and rupture is most likely controlled by their nucleation rates rather than growth, resulting in low final stress triaxiality values and small ε_n deformations.

Conclusions

The quantitative metallography done in this work measuring the volume fraction, size, and spacing of inclusions, gave the possibility to discriminate the fracture micromechanical processes of various 13% Cr-4% Ni martensitic stainless steels. Some correlations between material's microstructure, austenite content, failure features, and measured true fracture strains were explored using the modified Rice and Tracey model.

The conventional MVC mechanism was found as the main fracture mechanism after necking. The microstructural feature affecting the micromechanical processes during ductile rupture is the inclusion characteristics, and to some extent the matrix ductile behavior. The size and spacing of inclusions control the amount of void growth during necking. The measured stress triaxiality ratios using broken tension samples also showed that a higher void growth requires a higher stress triaxiality ratio.

In addition, various micromechanical scenarios were found in the studied metals. In the case of a rolled 415 steel, the MVC mechanism was interrupted by the formation of void sheets. Considering the radius of the initially nucleated micro-voids at the moment of void sheeting resulted in a better estimation of the deformation after necking. It was demonstrated that the formation of the void sheets in this steel inhibits the predicted true fracture strain to be attained by stopping the void growth and decreasing the constraint. The large inclusions found in the cast version (CA6NM) of this steel

were found to be the ones to initiate damage, but final rupture occurs thanks to the activation of much smaller inclusions. The very large number of potential microvoid nucleation sites found in weld metals limited the possibility for void growth and resulted in lower stress triaxiality ratio at rupture. This drastically reduced the strains after necking.

In the situation of the welded metals, the relationship between void growth and stress triaxiality ratio defined in the Rice and Tracey model is not efficient at describing the fracture behavior. Another element that is not taken in the Rice and Tracey model was considered when comparing the behavior of the as-welded and heat-treated metals: the effect of the matrix mechanical property. It was found that when applying an intercritical tempering heat treatment, the same amount of void growth took place, while larger true fracture strain was found in the softer matrix material. Even if the improvement is not significant (of the order to 13%) it shows that this parameter should be considered in further improvement of the Rice and Tracey model.

Acknowledgements Financial supports of Natural Science and Engineering Research Council of Canada (NSERC), Hydro-Québec, and Alstom Power Hydro are gratefully acknowledged. SEM, XRD and Rietveld analyses were performed at the Institut de Recherche d'Hydro-Québec (IREQ). The tension tests were carried out at École Polytechnique de Montréal under supervision of Mr. Yves Verreman. The authors of this paper would also like to thank Mrs. Manon Provencher, Mr. Étienne Dallaire, Mr. Alexandre Lapointe, technologists at IREQ, and Mrs. Josée Laviolette, technologist at École Polytechnique de Montréal for their valuable experimental assistance. Finally, we would like to express our warm thanks to Mr. Mathieu Paquin for the manufacture of the weld metal block of exceptional quality.

Compliance with ethical standards

Conflict of interest The authors declare that they have no conflict of interest.

References

Amrei MM, Monajati H, Thibault D, Verreman Y, Germain L, Bocher P (2016) Microstructure characterization and hardness distribution of 13Cr4Ni multipass weld metal. Mater Charact 111:128–136. https://doi.org/10.1016/j.matchar.2015.11.022

Anderson TL (2005) Fracture mechanics: fundamentals and applications. CRC Press, Boca Raton

Antolovich S (1996) Alloy design for fatigue and fracture, vol 19. ASM International, Cleveland

ASM-Handbook (2004) Quantitative characterization and representation of global microstructural geometry. In: Metallography and microstructures, vol 9. ASM-International, pp 428–447

ASTM-International (2009) Standard test methods for tension testing of metallic materials. ASTM, Cleveland

Benzerga AA, Leblond J-B (2010) Ductile fracture by void growth to coalescence. In: Hassan A, van der Erik G (eds) Advances in applied mechanics, vol 44. Elsevier, Amsterdam, pp 169–305. https://doi.org/10.1016/S0065-2156(10)44003-X

Bilmes P, Llorente C, Pérez Ipina J (2000) Toughness and microstructure of 13Cr4NiMo high-strength steel welds. J Mater Eng Perform 9:609–615

Bilmes P, Solari M, Llorente C (2001) Characteristics and effects of austenite resulting from tempering of 13Cr-NiMo martensitic steel weld metals. Mater Charact 46:285–296

Bridgman PW (1952) Studies in large plastic flow and fracture, vol 177. McGraw-Hill, New York

Brocks W, Schmitt W (1995) The second parameter in J-R curves: constraint or triaxiality?. In: Constraint effects in fracture theory and applications: Second Volume. ASTM International, Cleveland

Broek D (1971) A study on ductile fracture. Delft University of Technology, Delft

Campbell FC (2012) Fatigue and fracture: understanding the basics. ASM International, Cleveland

Carrouge D (2002) Phase transformations in welded supermartensitic stainless steels. University of Cambridge, Cambridge

Choudhary P, Garrison WM Jr (2010) The effect of inclusion type on the toughness of 4340 steel. Mater Manuf Process 25:180–184

Cox T, Low JR (1974) An investigation of the plastic fracture of AISI 4340 and 18 Nickel-200 grade maraging steels. Metall Trans 5:1457–1470

Das C, Albert S, Bhaduri A, Srinivasan G, Ramasubbu V (2008) Effect of minor change in composition on toughness of weldmetal for repair of turbine blades made of martensitic stainless steel. Sci Technol Weld Join 13:159–166

Dieter GE (1986) Mechanical metallurgy. McGraw-Hill series in materials science and engineering, 3rd edn. McGraw-Hill, New York

Escatha Y, Devaux J (1979) Numerical study of initiation, stable crack growth, and maximum load, with a ductile fracture criterion based on the growth of holes. In: Numerical Numerical study of initiation, stable crack growth, and maximum load, with a ductile fracture criterion based on the growth of holes

Folkhard E, Rabensteiner G (1988) Welding metallurgy of stainless steels. Springer, New York

Foroozmehr F, Verreman Y, Chen J, Thibault D, Bocher P (2017) Effect of inclusions on fracture behavior of cast and wrought 13% Cr-4% Ni martensitic stainless steels. Eng Fract Mech 175:262–278. https://doi.org/10.1016/j.engfracmech.2017.02.002

Franois D, Pineau A, Zaoui A (2012) Mechanical behaviour of materials: volume ii: fracture mechanics and damage, vol 191. Springer Science & Business Media, Berlin

Garrison WM Jr (2007) Controlling inclusion distributions to achieve high toughness in steels. Iron Steel Technol 4:132–139

Gurland J, Plateau J (1963) The mechanism of ductile rupture of metals containing inclusions. Trans ASM 56:442–454

Helbert AL, Feaugas X, Clavel M (1996) The influence of stress trlaxiality on the damage mechanisms in an equiaxed α/β Ti-6AI-4V alloy. Metall Mater Trans A 27:3043–3058. https://doi.org/10.1007/bf02663853

Hertzberg RW (1996) Deformation and fracture mechanics of engineering materials, 4th edn. Wiley, New York

Huang Y (1991) Accurate dilatation rates for spherical voids in triaxial stress fields. J Appl Mech 58:1084–1086

Lippold JC, Kotecki DJ (2005) Welding metallurgy and weldability of stainless steels. Wiley-Interscience, Hoboken

Maloney JL, Garrison WM (2005) The effect of sulfide type on the fracture behavior of HY180 steel. Acta Materialia 53:533–551

Maropoulos S, Ridley N, Kechagias J, Karagiannis S (2004) Fracture toughness evaluation of a H.S.L.A. steel. Eng Fract Mech 71:1695–1704. https://doi.org/10.1016/j.engfracmech.2003.08.006

McClintock FA (1968) A criterion for ductile fracture by the growth of holes. In: ASME

Pineau A (2008) Modeling ductile to brittle fracture transition in steels–micromechanical and physical challenges. Int J Fract 150:129–156. https://doi.org/10.1007/s10704-008-9232-4

Qiu H, Wang LN, Qi JG, Zuo H, Hiraoka K (2013) Enhancement of fracture toughness of high-strength Cr-Ni weld metals by strain-induced martensite transformation. Mater Sci Eng A 579:71–76. https://doi.org/10.1016/j.msea.2013.05.012

Rice JR, Tracey DM (1969) On the ductile enlargement of voids in triaxial stress fields $*$. J Mech Phys Solids 17:201–217

Rogers H (1960) The tensile fracture of ductile metals. AIME Trans 218:498–506

Schäfer L (1998) Influence of delta ferrite and dendritic carbides on the impact and tensile properties of a martensitic chromium steel. J Nucl Mater 258–263(Part 2):1336–1339. https://doi.org/10.1016/S0022-3115(98)00200-1

Shi YW (1989) Critical void growth for ductile rupture of steel welds. Eng Fract Mech 34:901–907. https://doi.org/10.1016/0013-7944(89)90226-9

Thibault D, Bocher P, Thomas M (2009) Residual stress and microstructure in welds of 13% Cr-4% Ni martensitic stainless steel. J Mater Process Technol 209:2195–2202

Thibault D, Bocher P, Thomas M, Gharghouri M, Côté M (2010) Residual stress characterization in low transformation temperature 13%Cr-4%Ni stainless steel weld by neutron diffraction and the contour method. Mater Sci Eng A 527:6205–6210. https://doi.org/10.1016/j.msea.2010.06.035

Thibault D, Bocher P, Thomas M, Lanteigne J, Hovington P, Robichaud P (2011) Reformed austenite transformation during fatigue crack propagation of 13%Cr-4%Ni stainless steel. Mater Sci Eng A 528:6519–6526. https://doi.org/10.1016/j.msea.2011.04.089

Trudel A, Lévesque M, Brochu M (2014) Microstructural effects on the fatigue crack growth resistance of a stainless steel CA6NM weld. Eng Fract Mech 115:60–72. https://doi.org/10.1016/j.engfracmech.2013.11.013

Young RA (1993) Introduction to the Rietveld method. In: Young RA (ed) The Rietveld method. Oxford University Press, Oxford, pp 1–38

Zhang S, Wang P, Li D, Li Y (2015) In situ investigation on the deformation-induced phase transformation of metastable austenite in Fe-13% Cr-4% Ni martensitic stainless steel. Mater Sci Eng A 635:129–132. https://doi.org/10.1016/j.msea.2015.03.084